

Subtle Tuning of Catalytic Well Effect in Phthalocyanine Covalent Organic Frameworks for Selective CO₂ Electroreduction into C₂H₄

Yi-Lu Yang, Qi Li, Ping Liu, Qing Xu, Qi-Yi Zeng, Yu-Xin Chen, Yu-Qing Yang, Hao-Tao Yang, Fei Yu,* Yi-Rong Wang,* Yifa Chen,* and Ya-Qian Lan

In the electrocatalytic CO₂ reduction reaction (CO₂RR), the strategic design of a catalytic well capable of regulating the overall confinement effects of catalytic sites holds significant promise for enhancing multiple-electron transfer and C–C coupling efficiency, particularly for the generation of C₂₊ products. Here, a series of Cu-salphen-based covalent organic frameworks (COFs) featuring hydroxyl-induced catalytic well are synthesized, which demonstrate successful application in electrocatalytic CO₂RR to yield multiple-electron transferred products. The meticulously engineered catalytic well, facilitated by multi-hydroxyl groups, manifests robust confinement effects, facilitating selective adsorption, enrichment, and activation of CO₂, intermediate stabilization, and reduction of energy barriers for electrocatalytic CO₂RR. Specifically, product selectivity can be finely tuned from CH₄ to C₂H₄ by modulating the levels of catalytic well, with CuPc-DFP-4OH-Cu exhibiting the most pronounced catalytic well effect, yielding a high 56.86% faradaic efficiency (FE) for C₂H₄ at –0.7 V, while CuPc-DFP-Cu, with the weakest catalytic well effect, achieves a 75.24% FE for CH₄ at –1.0 V. Notably, the attained FE for C₂H₄ (56.86%) surpasses that of all reported COFs to date. Complemented by theoretical calculations and in situ tests, this study delves deeply into the pivotal roles of hydroxyl-induced catalytic well with confinement effects.

CH₄, C₂H₄, ethanol, and others, utilizing renewable electricity as a trigger. This process offers an alternative approach to closing the carbon loop.^[1–3] Among various metal-based catalysts reported, copper-based catalysts exhibit distinctive electrocatalytic capabilities and are widely explored for the production of diverse C₂₊ products, including hydrocarbons and alcohols.^[4–11] Ideally, a copper-based catalyst for generating C₂₊ products should possess several key properties, including efficient CO₂ adsorption, enrichment, and activation,^[12,13] high electron conductivity, multiple-electron transfer capability,^[14,15] and well-tuned microenvironments of active sites.^[16,17] However, despite significant progress, the achieved efficiencies for C₂₊ products remain unsatisfactory, necessitating a deeper mechanistic understanding to guide the design of efficient copper-based electrocatalysts.^[18,19] Particularly, microenvironmental tuning of copper-based active sites significantly influences the charge density distribution of catalytic centers and interactions

1. Introduction

The electrocatalytic reduction of carbon dioxide (CO₂RR) presents considerable potential for converting chemically inert CO₂ into value-added products such as CO, formic acid,

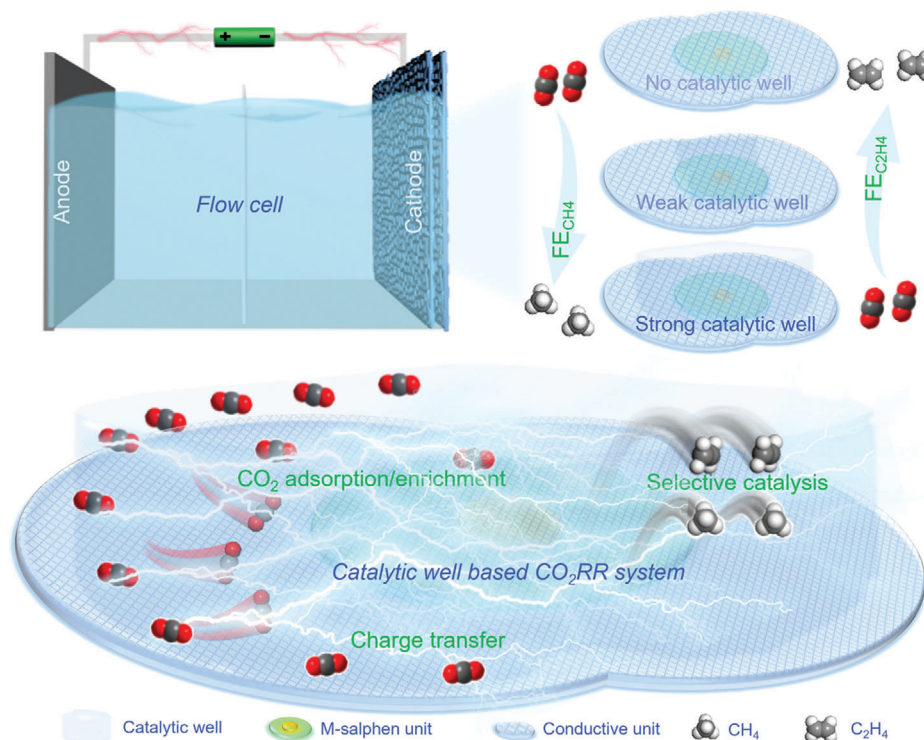
with intermediate species, thereby determining product efficiency. Nevertheless, existing studies on microenvironmental tuning of copper-based catalysts predominantly focus on C₁ products, with limited exploration of C₂₊ products.^[20–23] Therefore, establishing well-defined catalytic systems to elucidate the impact of microenvironments on C₂₊ product formation is crucial for unveiling the intrinsic catalytic nature of copper-based catalysts.

Covalent organic frameworks (COFs) represent a class of covalent-bond based porous crystalline materials with superior properties such as well-defined architectural structures, accessible pore channels, tunable structures, and functions.^[24–26] Owing to these advantages, COFs have emerged as promising candidates for electrocatalytic CO₂ reduction reactions (CO₂RR), as evidenced by numerous studies.^[27–32] However, most reported products are limited to C₁ species, with the efficient production of C₂₊ products are remaining elusive due to the scarcity of Cu-based COFs featuring suitable active sites or microenvironments conducive to C–C coupling reactions.^[33–36] To address these bottlenecks, we propose the concept of a catalytic well for microenvironment tuning of active sites with Cu-based COFs

Y.-L. Yang, Q. Li, Q. Xu, Q.-Y. Zeng, Y.-X. Chen, Y.-Q. Yang, H.-T. Yang, Y.-R. Wang, Y. Chen, Y.-Q. Lan
School of Chemistry
South China Normal University
Guangzhou 510006, P. R. China
E-mail: yirongwang@m.scnu.edu.cn; 20200698@m.scnu.edu.cn
P. Liu, F. Yu
School of Chemistry and Materials Science
Nanjing Normal University
Nanjing 210023, P. R. China
E-mail: feiyu@njnu.edu.cn

The ORCID identification number(s) for the author(s) of this article can be found under <https://doi.org/10.1002/adma.202415799>

DOI: 10.1002/adma.202415799



Scheme 1. Schematic illustration of the advantages of catalytic well effect on selective catalysis in electrocatalytic CO₂RR.

platforms. By designing a catalytic well with robust confinement effects to synergize with Cu active sites in Cu-based COFs, enhanced interactions CO₂ adsorption/enrichment/activation or intermediate stabilization interactions may be induced, thereby facilitating C-C coupling reactions and the production of C₂₊ products. Theoretical considerations underscore the appeal of designing such catalytic well-incorporated Cu-based COFs for gaining insights into electrocatalytic CO₂RR toward C₂₊ products. Nonetheless, constructing suitable Cu-based COF platforms to meet these requirements remains a formidable challenge.

As a proof-of-concept, we synthesized a series of Cu-salphen based COFs (CuPc-DFP-*n*OH-Cu, *n* = 0, 2, and 4) featuring varying levels of hydroxyl-induced catalytic well, aimed at selective electrocatalytic CO₂RR (**Scheme 1**). The concept of catalytic well proposed in this work is a kind of space confinement effect induced by multiple hydroxyl groups around the catalytic sites.^[37,38] It is a kind of interesting concept derived from the space confinement effects that are based on the obtained COFs in this work. The meticulously designed catalytic well, facilitated by multi-hydroxyl groups, exhibits pronounced site-confinement effects, enabling selective adsorption, enrichment, and activation of CO₂, as well as intermediate stabilization and reduced energy barriers for electrocatalytic CO₂RR. Notably, the products can be well tuned from CH₄ to C₂H₄ by introducing different levels of catalytic well. Specifically, CuPc-DFP-4OH-Cu, exhibiting the most robust catalytic well effect, achieves a high faradaic efficiency (FE) of 56.86% for C₂H₄ at −0.7 V, while CuPc-DFP-Cu, with the weakest catalytic well effect, demonstrates a FE of 75.24% for CH₄ at −1.0 V.

2. Results

2.1. Synthesis and Structure of CuPc-DFP-*n*OH-Cu (*n* = 0, 2, and 4)

To prepare CuPc-DFP-*n*OH-Cu (*n* = 0, 2, and 4), CuPc-DFP-*n*OH (*n* = 0, 2, and 4) were first prepared through the Schiff base condensation of CuPc-8NH₂ and related monomers (**Figure 1a**, detail see Experimental Section). Taking CuPc-DFP-4OH-Cu as an example, CuPc-DFP-4OH was first prepared through the condensation of CuPc-8NH₂ and 2, 4-dimethoxyacetylphloroglucinol (DFP-2OH) and further modification process of metal acetate salts for further characterizations (**Figure S1**, Supporting Information). An *Amm2* space group based on CuPc-DFP-4OH-Cu has been built and performed Le Bail refinements of the PXRD patterns for full profile fitting against the proposed models, in which the powder X-ray diffraction (PXRD) pattern obtained from the simulated structure matches well with the experimental results (*R*_{wp} = 2.92% and *R*_p = 2.21%) (**Figure 1d**; **Table S1**, Supporting Information). PXRD pattern and simulation results show an AA packing model with *Amm2* space group for CuPc-DFP-4OH-Cu (**Figure 1d**), and its unit cell parameters are *a* = *b* = 25.1103 Å, *c* = 3.4422 Å, *α* = *β* = *γ* = 90°. Besides, the simulated crystal structure shows that the layer distance of CuPc-DFP-4OH-Cu is 3.44 Å. Moreover, CuPc-DFP-*n*OH-Cu (*n* = 0 and 2) with iso-reticular structures when compared with CuPc-DFP-4OH-Cu have also been detected and their high crystallinity was proved by the PXRD patterns (**Figures 1b,c** and **S2**, **Tables S2** and **S3**, Supporting Information). Thus, we have obtained three kinds of COFs (CuPc-DFP-*n*OH-Cu, *n* = 0, 2, and 4) constructed by

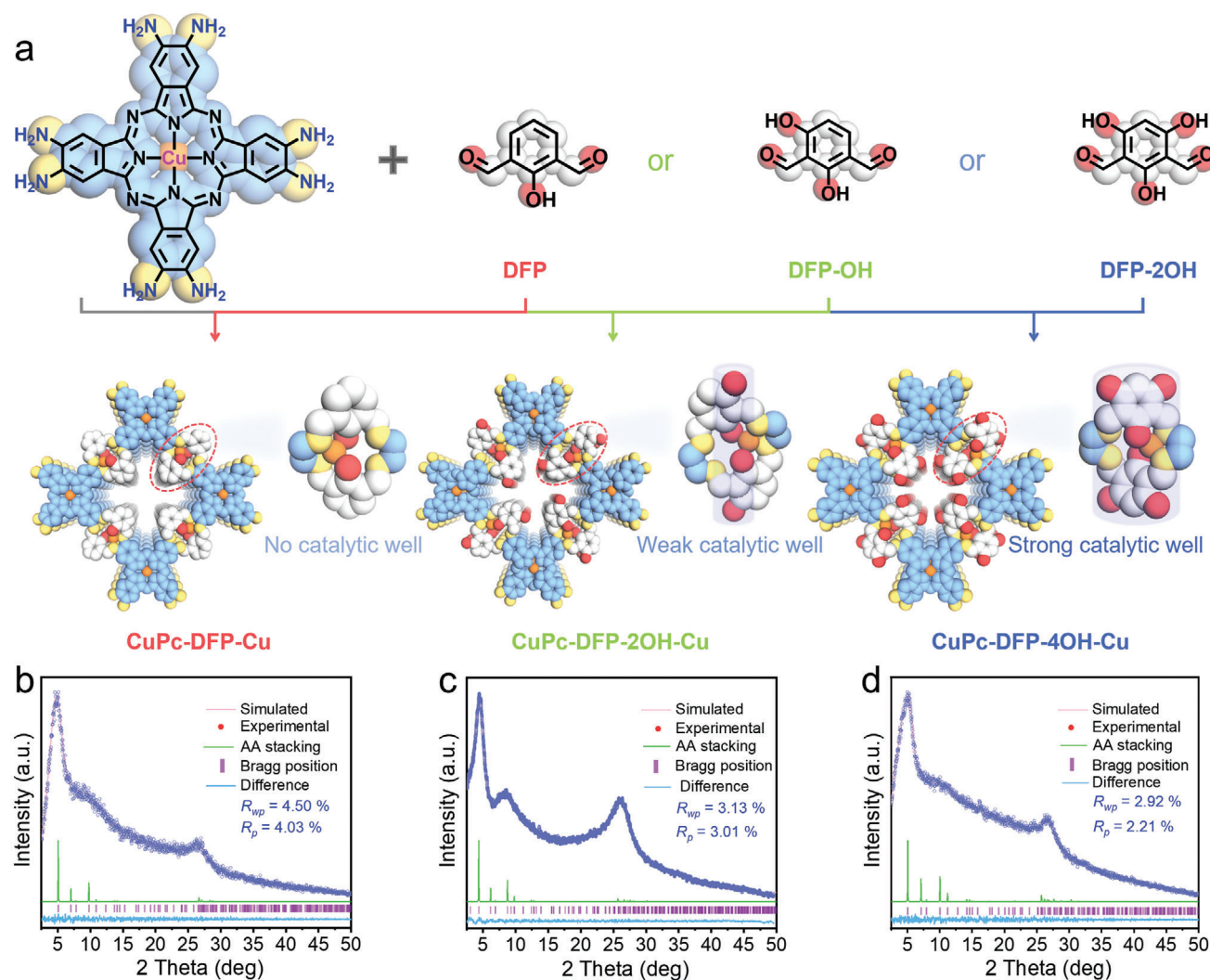


Figure 1. Structure and characterization of CuPc-DFP-nOH-Cu ($n = 0, 2$, and 4). a) The syntheses and structures of CuPc-DFP-nOH-Cu ($n = 0, 2$, and 4). b) Experimental (blue dot) and simulated (pink line) PXRD patterns of CuPc-DFP-Cu. c) Experimental (blue dot) and simulated (pink line) PXRD patterns of CuPc-DFP-2OH-Cu. d) Experimental (blue dot) and simulated (pink line) PXRD patterns of CuPc-DFP-4OH-Cu.

Cu-salphen and Cu-Pc units, in which different numbers of hydroxyl groups are modified around Cu-salphen units that might be ideal structure platforms for electrocatalytic CO_2 RR.

In addition, the Fourier transform infrared spectroscopy (FT-IR) tests have been performed to study their components. In the FT-IR spectrum of CuPc-DFP-4OH-Cu, the $\text{C}=\text{O}$ stretching band at 1683 cm^{-1} of DFP-2OH and the $\text{N}-\text{H}$ stretching band at $3199\text{--}3350\text{ cm}^{-1}$ of CuPc- 8NH_2 monomer disappear along with the appeared $\text{C}=\text{N}$ stretching vibration band at 1619 cm^{-1} , indicating the generation of $\text{C}=\text{N}$ bond. Besides, a new peak observed at $\approx 1600\text{ cm}^{-1}$ belongs to the metal co-ordinated $\text{C}=\text{N}$ groups in the salphen pockets, which indicates the successful synthesis of CuPc-DFP-4OH-Cu (Figure 2a).^[39] Similar results have also been detected for CuPc-DFP-nOH-Cu ($n = 0$ and 2) (Figures S3 and S4, Supporting Information). Moreover, ^{13}C solid-state NMR spectroscopy (^{13}C ssNMR) was conducted to further confirm the structure. The characteristic peak at 153.1 ppm (i.e. e) is ascribed to the carbon atom

of $\text{C}=\text{N}$ bond for CuPc-DFP-4OH-Cu.^[39] Meanwhile, other detected peaks can be assigned to phthalocyanine (i.e. a, b, c, and d) or DFP-2OH (i.e. f, g, h, and i) (Figure S5a, Supporting Information). Similar results have also been detected for CuPc-DFP-nOH-Cu ($n = 0$ and 2) (Figure S5b,c, Supporting Information).

Based on the obtained structures of CuPc-DFP-nOH-Cu ($n = 0, 2$, and 4), they possess iso-reticular structures while imparting varied amounts of hydroxyl groups. To evaluate the possible effect of the hydroxyl group on the CO_2 adsorption properties of CuPc-DFP-nOH-Cu ($n = 0, 2$, and 4), CO_2 adsorption tests have been carried out. The results display that the CO_2 adsorption capacity of CuPc-DFP-4OH-Cu ($69.9\text{ cm}^3\text{ g}^{-1}$) is higher than that of CuPc-DFP-2OH-Cu ($24.0\text{ cm}^3\text{ g}^{-1}$) and CuPc-DFP-Cu ($17.2\text{ cm}^3\text{ g}^{-1}$) at 273 K (Figure 2b). Interestingly, the CO_2 adsorption enthalpy of CuPc-DFP-4OH-Cu is higher than that of CuPc-DFP-2OH-Cu and CuPc-DFP-Cu, indicating its more favored interaction with CO_2 (Figures S6 and S7, Supporting Information).

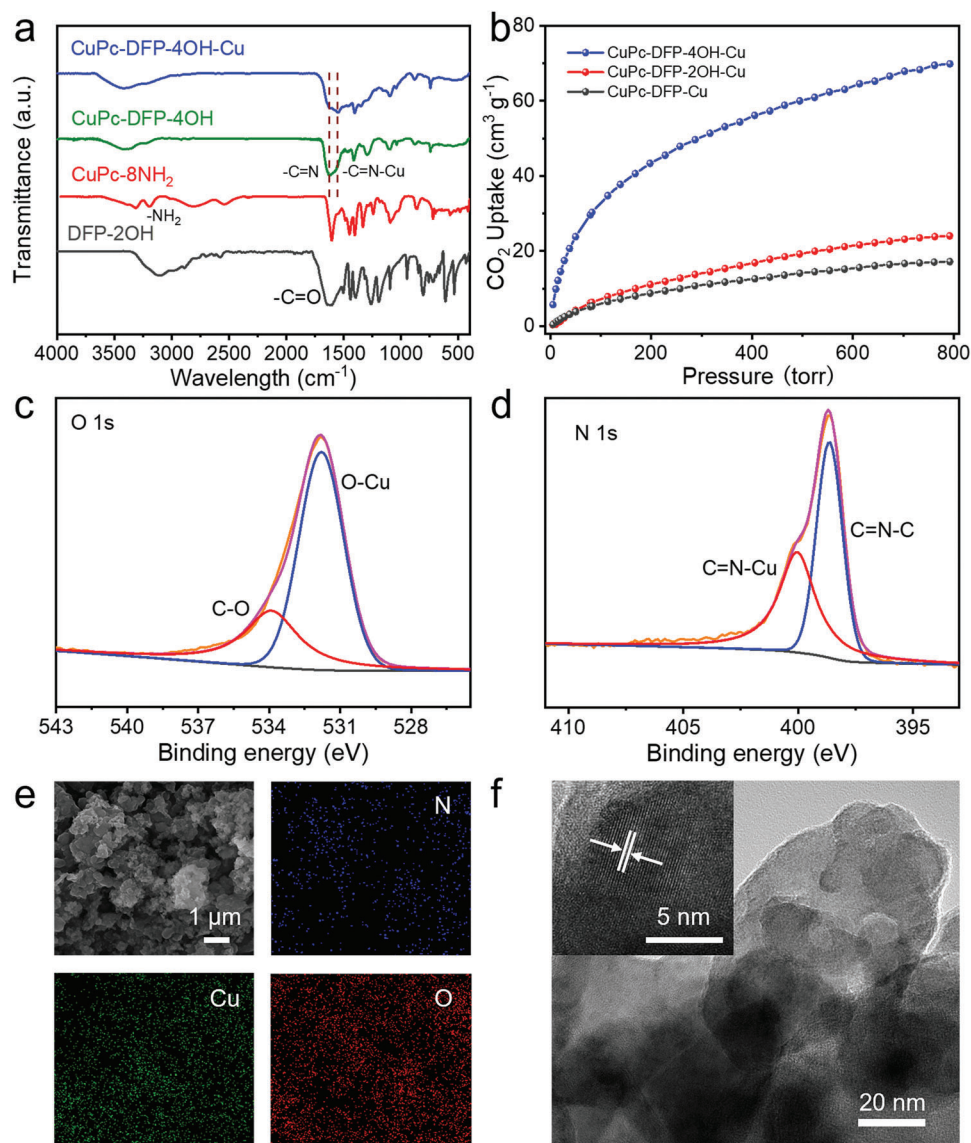


Figure 2. The characterizations of CuPc-DFP-4OH-Cu. a) The FT-IR spectra of CuPc-DFP-4OH-Cu. b) CO_2 adsorption curves of CuPc-DFP- $n\text{OH-Cu}$ ($n = 0, 2$, and 4) at 273 K . c) Survey scan XPS profiles of $\text{O } 1s$ for CuPc-DFP-4OH-Cu. d) Survey scan XPS profiles of $\text{N } 1s$ for CuPc-DFP-4OH-Cu. e) The SEM and elemental mapping images of CuPc-DFP-4OH-Cu. f) The TEM and HRTEM (insert) images of CuPc-DFP-4OH-Cu (the lattice spacing is 0.25 nm).

To study the chemical states of the elements in these COFs, X-ray photoelectron spectroscopy (XPS) was conducted. The $\text{O } 1s$ XPS spectrum of CuPc-DFP-4OH-Cu is fitted into two peaks that belong to C-O and Cu-O , respectively, meanwhile, only a single peak is detected for CuPc-DFP-4OH (Figure 2c; Figures S8 and S9, Supporting Information). In the $\text{Cu } 2p$ high-resolution spectrum, the binding energies detected at 934.7 and 954.6 eV are attributed to $\text{Cu } 2p_{3/2}$ and $\text{Cu } 2p_{1/2}$, respectively, consistent with the Cu(II) state (Figure S9, Supporting Information).^[25] Besides, the XPS spectra of the CuPc-DFP-4OH-Cu show that the $\text{N } 1s$ spectrum can be fitted into C-N=C (398.6 eV) and C=N-Cu (400.6 eV), which confirms the existence of Cu-N bond (Figure 2d).^[39] Besides, the $\text{N } 1s$ spectra of CuPc-DFP- $n\text{OH-Cu}$ ($n = 0$ and 2) exhibit a slight offset when compared with CuPc-

DFP-4OH-Cu (Figures S10 and S11, Supporting Information). To detect the actual Cu content, the inductively coupled plasma emission spectrometer (ICP-OES) was carried out. It displays that the specific Cu contents in CuPc-DFP-4OH-Cu, CuPc-DFP-2OH-Cu, and CuPc-DFP-Cu are detected to be 12.44% , 13.56% and 13.71% , respectively, which is slightly lower than theoretical values and indicates the single Cu coordinated in the salphen pockets (Table S4, Supporting Information).

In addition, the obtained CuPc-DFP-4OH-Cu displays a kind of nanoparticle morphology (diameter, $340\text{--}440\text{ nm}$) as proved by the scanning electron microscopy (SEM) and transmission electron microscopy (TEM) tests (Figure 2e,f). Energy dispersive X-ray spectroscopy (EDS) mapping images certify that the elements are uniformly distributed (Figure 2e). In the HR-TEM image

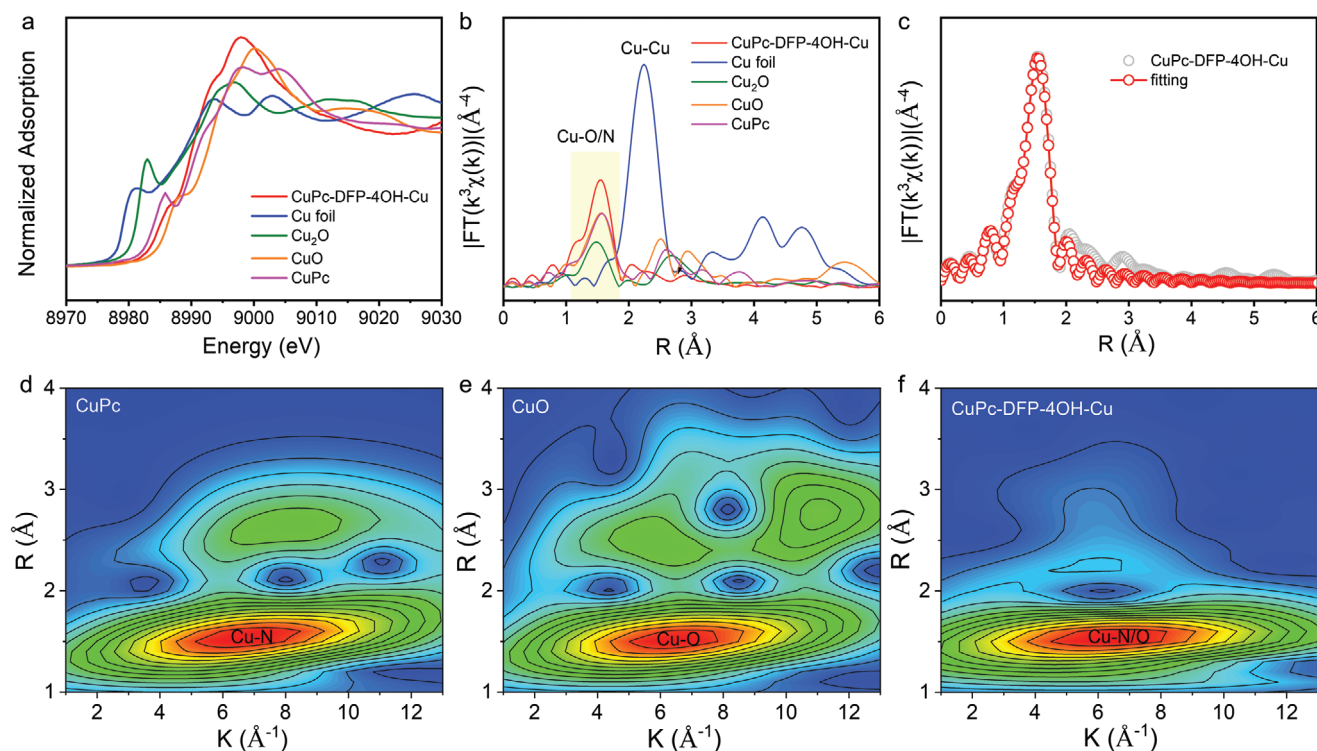


Figure 3. XAS spectra. a) Cu K-edge of XANES spectra of CuPc-DFP-4OH-Cu, Cu foil, CuPc, Cu₂O, and CuO. b) Cu K-edge of EXAFS spectra of CuPc-DFP-4OH-Cu, Cu foil, CuPc, Cu₂O, and CuO. c) Corresponding EXAFS fitting curves for CuPc-DFP-4OH-Cu. d) Cu K-edge WT-EXAFS spectra of CuPc. e) Cu K-edge WT-EXAFS spectra of CuO. f) Cu K-edge WT-EXAFS spectra of CuPc-DFP-4OH-Cu.

of CuPc-DFP-4OH-Cu, obvious lattice fringes are obviously visible, which confirms its high crystallinity (Figure 2f). In comparison, the morphology of contrast samples like CuPc-DFP-2OH-Cu, CuPc-DFP-Cu, and CuPc-DFP-4OH have also been tested and all exhibit nanoparticle morphology (Figures S12–S14, Supporting Information).

Synchrotron-radiation-based X-ray absorption spectroscopy (XAS) has been further applied to elucidate the electronic structure and local information of Cu atom in CuPc-DFP-4OH-Cu (Figure 3). For the Cu K-edge X-ray absorption near-edge structure (XANES) (Figure 3a), the absorption edge of CuPc-DFP-4OH-Cu is close to that of CuO, implying the positive valence state of Cu in CuPc-DFP-4OH-Cu is +2, which is in accordance with the XPS results. The Cu K-edge FT-EXAFS spectra present a main peak at ≈ 1.53 Å, which lies between the Cu–N in copper phthalocyanine (CuPc) and the Cu–O in the CuO scattering path, proving that the Cu center of CuPc-DFP-4OH-Cu is coordinated by both N and O atoms (Figure 3b). Additionally, the Cu K-edge XANES and FT-EXAFS spectra of CuPc-DFP-4OH-Cu are close to that of CuPc, indicating that the CuPc-DFP-4OH-Cu has a similar Cu microenvironment as that of CuPc (Figure 3a–c). Importantly, no Cu–Cu bond (Cu foil) at ≈ 2.24 Å is observed, corroborating the atomic dispersion of Cu site in CuPc-DFP-4OH-Cu, which has been further confirmed by the wavelet-transform spectrum of the k^3 -weighted EXAFS (WT-EXAFS) (Figure 3d–f; Figure S15, Supporting Information). In addition, the XAS spectra of CuPc-DFP-4OH-Cu, Cu K-edge XANES, and FT-EXAFS verify that the fine detail of Cu atom in CuPc-DFP-4OH-Cu contains both Cu–N and Cu–O coordination modes with Cu²⁺ oxida-

tion state (Table S5, Supporting Information). To elucidate the number of metal ions in the salphen units, we have simulated the structural model with two metal ions in the salphen pockets. Considering that if two metal ions were inserted into the salphen unit, there would be a scattering path of adjacent metal-metal bonding in Fourier transformed extended X-ray absorption fine structure (FT-EXAFS) spectra. Obviously, no metal-metal bonding peak (around 2.24 Å) is observed in the experimental FT-EXAFS spectra of CuPc-DFP-4OH-Cu (Figure 3b), excluding the possibility that two adjacent metal ions exist in the Cu-salphen units of CuPc-DFP-4OH-Cu. These analyses further support the backbone structure of CuPc-DFP-4OH-Cu and confirm that each salphen pocket basically incorporates one metal ion. In addition to these, the inductively coupled plasma mass spectrometry (ICP-MS) analysis indicates that the specific content of Cu element in CuPc-DFP-4OH-Cu is 12.44% (Table S4, Supporting Information). The lower metal content than the theoretical one (13.87%) might be probably due to the residual end groups on the edges or defects in the extended structures.

To test the durability of CuPc-DFP-4OH-Cu, the sample was soaked in different solvents (i.e. dichloromethane (DCM), N, N-dimethylformamide (DMF), MeOH, KOH (1 M) and HCl (1 M)) for one week. The PXRD patterns of CuPc-DFP-4OH-Cu after stability tests exhibit remained structure when compared with the initial state (Figure S16, Supporting Information). Besides, thermogravimetric analysis (TGA) tests have been performed under oxygen atmosphere to evaluate the thermal stability. CuPc-DFP-*n*OH-Cu (*n* = 0, 2, and 4) and CuPc-DFP-4OH all exhibit high thermal stability with slight weight loss up to ≈ 200 °C, revealing

its high stability that might be much favorable for electrocatalytic CO₂RR (Figure S17, Table S6, Supporting Information).

2.2. The Electrocatalytic Properties of CuPc-DFP-nOH-Cu ($n = 0, 2$, and 4)

To test the electrocatalytic performance, the catalysts are evaluated in a three-electrode flow cell system at selected potentials. The gaseous products of CuPc-DFP-nOH-Cu ($n = 0, 2$, and 4) were monitored by gas chromatography (GC) and liquid products were analyzed by ¹H nuclear magnetic resonance spectroscopy (¹H-NMR). The results show that no liquid products like ethanol were detected in the electrocatalytic CO₂RR systems (Figure S18, Supporting Information), possibly due to their unmet structure properties for liquid product formation.^[40]

To evaluate the selectivity of samples for hydrogen evolution reaction (HER) and electrocatalytic CO₂RR, Linear sweep voltammetry (LSV) curves of CuPc-DFP-nOH-Cu ($n = 0, 2$, and 4) samples were scanned under Ar and CO₂ atmospheres in the range of -1.2 – 0 V. The results show that CuPc-DFP-4OH-Cu, CuPc-DFP-2OH-Cu, and CuPc-DFP-Cu possess a total current density of -108.7 , -85.2 , and -62.5 mA cm⁻² at -0.7 V, respectively (Figure 4a). In electrocatalytic CO₂RR, CuPc-DFP-4OH-Cu, CuPc-DFP-2OH-Cu, and CuPc-DFP-Cu all display much higher current density than that in HER, indicating they all strongly favor the electrocatalytic CO₂RR than HER (Figure 5a; Figure S19, Supporting Information). At -0.7 V, CuPc-DFP-4OH-Cu has higher FE_{C₂H₄} (FE_{C₂H₄}, 56.86%) than that of CuPc-DFP-2OH-Cu (FE_{C₂H₄}, 35.74%) and CuPc-DFP-Cu (FE_{C₂H₄}, 15.36%) (Figure 4b,c). The achieved excellent electrocatalytic CO₂RR performance (FE_{C₂H₄} = 56.86%, -0.7 V) is superior to all the currently reported COFs in electrocatalytic CO₂RR (Figure 4e; Table S7, Supporting Information).^[36,49–52] Besides, the FE_{C₂H₄+CH₄} of CuPc-DFP-4OH-Cu keeps higher than 57.8% in the wide range of potentials (-0.7 to -1.2 V) (Figure 5b,c). Meanwhile, the trend of C₂H₄ current density ($j_{C_2H_4}$) is consistent with that of FE_{C₂H₄} for CuPc-DFP-nOH-Cu ($n = 0, 2$, and 4) (Figure 4c), which indicates the important role of hydroxyl-induced catalytic well in enhancing the FE_{C₂H₄} and $j_{C_2H_4}$ during the electrocatalytic CO₂RR. Interestingly, the FE_{CH₄} displays an opposite trend in contrast to FE_{C₂H₄} for samples from CuPc-DFP-Cu to CuPc-DFP-4OH-Cu. For example, the FE_{CH₄} values of CuPc-DFP-4OH-Cu, CuPc-DFP-2OH-Cu, and CuPc-DFP-Cu are 13.79%, 19.09% and 44.30% at -0.7 V, and slightly increase to 37.02%, 52.54% and 75.24% at -1.0 V, respectively, which show different trend when compared with FE_{C₂H₄} values (Figures S20–S22, Supporting Information).

In contrast to CuPc-DFP-4OH-Cu, the main product of CuPc-DFP-4OH is H₂ (Figure S23, Supporting Information), which proves that the main active site is Cu salphen unit for electrocatalytic CO₂RR. Besides, the FE_{C₂H₄+CH₄} of CuPc-DFP-4OH-Cu reaches up to 70.65% at -0.7 V, which is significantly higher than that of CuPc-DFP-2OH-Cu (54.83%) and CuPc-DFP-Cu (59.66%) at the same potential (Figure 4b). Specifically, CuPc-DFP-2OH-Cu with moderate FE_{C₂H₄} and FE_{CH₄}, present the highest FE_{C₂H₄+CH₄} (93.54%) at -1.0 V (Figure 4b). Moreover, a radar chart of the performances for CuPc-DFP-nOH-Cu ($n = 0, 2$, and 4) in C₂H₄ generation based on the electrocatalytic CO₂RR

results at -0.7 V was made (Figure 4f; Table S8, Supporting Information). In detail, the energy efficiency (EE) of C₂H₄ for CuPc-DFP-4OH-Cu is calculated to be 34%, which is higher than that of CuPc-DFP-2OH-Cu (21%) and CuPc-DFP-Cu (9%) at -0.7 V (Figure 4d). Besides, with the increase of hydroxyl-induced catalytic well level, the total current density of electrocatalytic CO₂RR and turnover frequency (TOF) of C₂H₄ were significantly increased. Notably, the achieved TOF of CuPc-DFP-4OH-Cu (155.91 h⁻¹) for C₂H₄ generation is almost two times higher than that of CuPc-DFP-Cu (80.89 h⁻¹) (Figure 4f and Table S8, Supporting Information). In addition, the electrochemical impedance spectroscopy (EIS) of CuPc-DFP-nOH-Cu ($n = 0, 2$, and 4) at -0.7 V has been tested. The results show that the electronic transmission resistance of CuPc-DFP-4OH-Cu, CuPc-DFP-2OH-Cu, and CuPc-DFP-Cu were evaluated to be 1.33, 6.23, and 10.28 Ω, respectively (Figure S24, Supporting Information), implying the faster electron transfer efficiency of CuPc-DFP-4OH-Cu.

Furthermore, the isotopic-labeling experiments were carried out to prove the source of the gas products and the products have been analyzed by GC-MS using ¹³CO₂ as substrate under identical reaction conditions. The peaks at $m/z = 17$, 29, and 30 are attributed to ¹³CH₄, ¹³CO, and ¹³C₂H₄, respectively, confirming that the gas products indeed come from CO₂ (Figure 5d; Figure S25, Supporting Information). Besides, to test the electrochemical stability of the catalyst, the i-t test was carried out at -0.7 V for 3600 s (Figure 5e). During the stability test, the current density remains intact with slightly decreased FE_{C₂H₄}, proving its good stability in the electrochemical test. Furthermore, as verified by the PXRD test, CuPc-DFP-4OH-Cu displays remained peaks when compared to the state before test (Figure S26, Supporting Information). Further proved by the ICP leaching test, negligible leaching metal ions are detected in the solution after electrocatalytic CO₂RR (Table S9, Supporting Information), which shows there are no free Cu(II) ions dissolved in the electrolyte. Moreover, the XPS tests after CO₂RR show that the surface electronic state and elemental composition of the electronic structure remain unchanged (Figure S27, Supporting Information). The observed Cu 2p_{3/2} binding energy of 934.7 eV and 2p_{1/2} binding energy of 954.6 eV are consistent with Cu (II). There are no Cu and Cu(I) observed, which further proves the stability of the catalyst after CO₂RR.

2.3. Investigating the Structure-Function Relationships

To further explore the origin of the electrocatalytic CO₂RR process, the in situ ATR-FTIR measurements were performed to detect the intermediates. During the tests, the absorption peaks of *COOH (OH deformation of *COOH, 1250 cm⁻¹; symmetric stretch of *COOH, 1397 cm⁻¹; asymmetric stretch of *COOH, 1559 cm⁻¹) emerge (Figure 6a), which indicate the occurrence of CO₂ hydrogenation. In addition, intermediates (i.e. *CHO, 1053 cm⁻¹; *CH₂O, 1475 cm⁻¹ and CO (*CO), 2090 cm⁻¹) that are regarded as the key intermediates for the CH₄ formation have been detected.^[41] Meanwhile, *CO-CHO (1542 cm⁻¹) and *CO-CH₂ (1486 cm⁻¹) have also been detected, which are key intermediates for C–C coupling reaction in the generation of C₂H₄ (Figure 6a,b).^[42,43,44] These results support the electrocatalytic

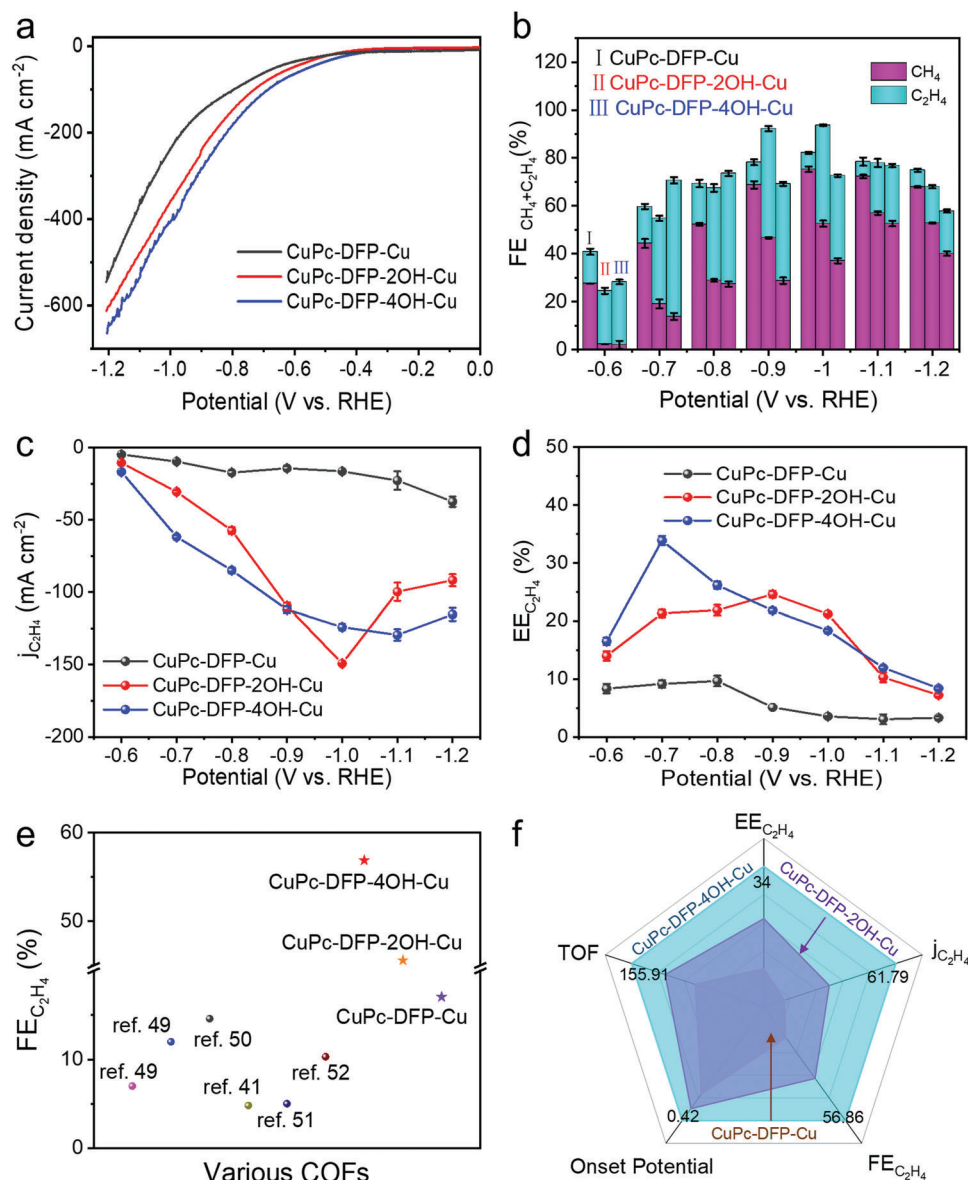


Figure 4. The electrocatalytic CO₂RR performances for CuPc-DFP-nOH-Cu ($n = 0, 2$, and 4). a) LSV curves of CuPc-DFP-nOH-Cu ($n = 0, 2$, and 4). b) FE_{CH₄+C₂H₄} of CuPc-DFP-nOH-Cu ($n = 0, 2$, and 4). c) Partial CH₄ current density of CuPc-DFP-nOH-Cu ($n = 0, 2$, and 4). d) Energy efficiency of CuPc-DFP-nOH-Cu ($n = 0, 2$, and 4). e) A summary of electrocatalytic performances of the literature based on COFs reported materials and CuPc-DFP-nOH-Cu ($n = 0, 2$, and 4). f) The radar chart of performance comparison for CuPc-DFP-nOH-Cu ($n = 0, 2$, and 4) (TOF, h⁻¹; EE, %; j_{C₂H₄}, mA cm⁻²; FE_{C₂H₄}, %; Onset Potential, V).

ability of CuPc-DFP-4OH-Cu in the conversion of CO₂ into CH₄ or C₂H₄, which also complies with the experimental data.

To further evaluate the interaction of CO₂ with CuPc-DFP-nOH-Cu ($n = 0, 2$, and 4), the radial distribution function ($g(r)$) was calculated, which can help to provide insights into the correlation between atomic pairs.^[45] The $g(r)$ function was scrutinized for the hydroxyl groups of COFs in interacting with CO₂ via molecular dynamics simulation, adhering to established conditions (Figure 6c; Videos S1–S3, Supporting Information). The cutoff radius for the radial distribution function $g(r)$ is determined by centering on the H atom at the relevant position. Specifically, for CuPc-DFP-Cu, the H atom on the corresponding ben-

zene ring is used as the reference point. For CuPc-DFP-2OH-Cu and CuPc-DFP-4OH-Cu, the H atom on the corresponding OH group is used as the reference point. Besides, the cut-off radius of $g(r)$ is 10 Å. Within the radius range of 1.75–2.75 Å, a notable escalation in the $g(r)$ values of COFs was observed. Specifically, the rate of increase for CuPc-DFP-4OH-Cu surpasses that of CuPc-DFP-2OH-Cu, while the latter exhibits a higher rate of increase compared to CuPc-DFP-Cu. This disparity suggests that the CO₂ interaction in CuPc-DFP-4OH-Cu is stronger than that of CuPc-DFP-2OH-Cu and CuPc-DFP-Cu. This finding strongly corroborates the significant role of hydroxyl-induced catalytic well in CO₂ interaction, aligning with the experimental data. Hence, the

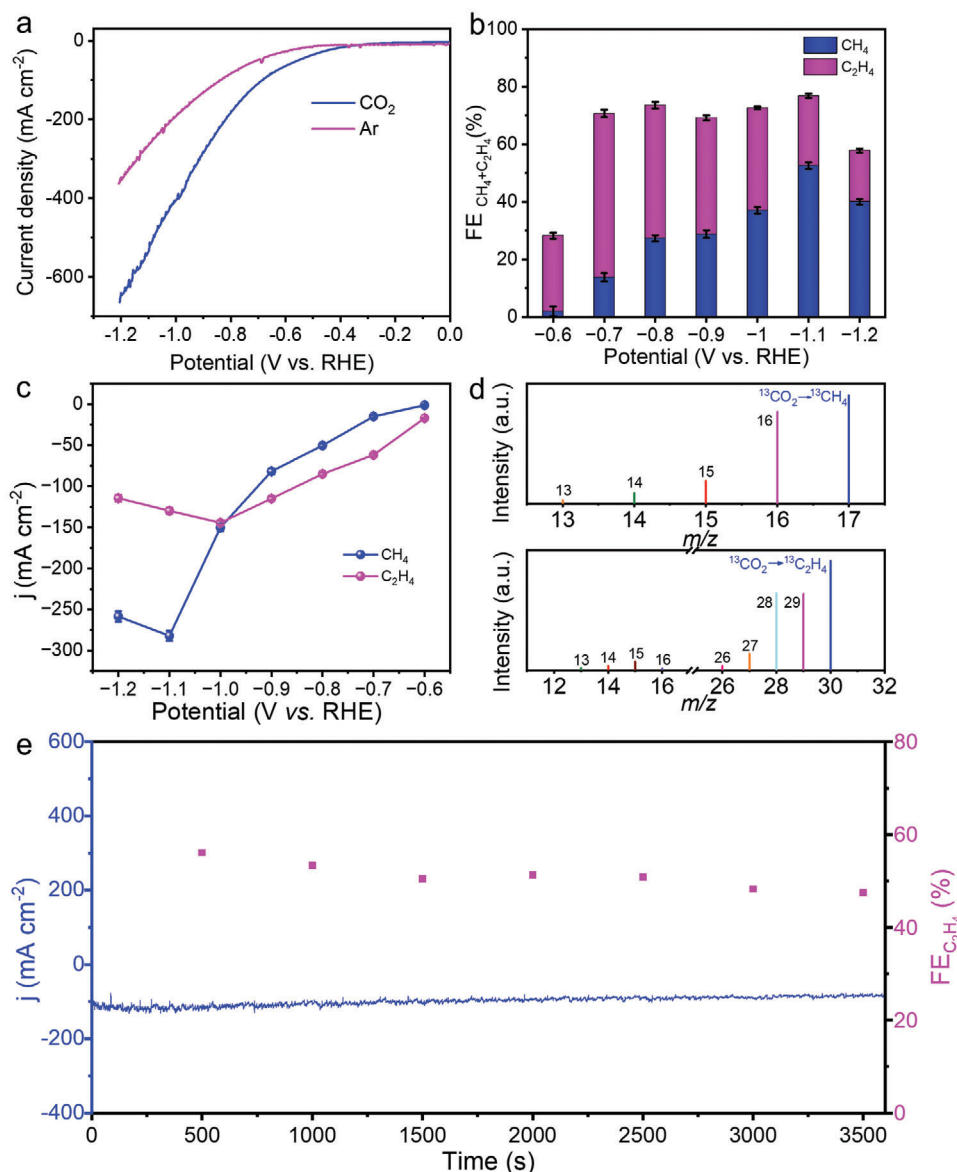


Figure 5. Evaluation of the electrocatalytic CO₂RR performance for CuPc-DFP-4OH-Cu in electrochemical measurements. a) Comparison of LSV curves of CuPc-DFP-4OH-Cu under CO₂ and Ar conditions. b) FE_{CH₄+C₂H₄} of CuPc-DFP-4OH-Cu at different potentials. c) Partial CH₄ and C₂H₄ current density of CuPc-DFP-4OH-Cu. d) The mass spectra of ¹³CH₄ and ¹³C₂H₄ recorded under ¹³CO₂ atmosphere. e) Durability test of CuPc-DFP-4OH-Cu at -0.7 V.

pronounced affinity of the strong affinity of hydroxyl-induced catalytic well toward CO₂ significantly enhances the initial step of CO₂ adsorption and enrichment during the electrocatalytic CO₂RR, thereby augmenting the likelihood of C-C coupling. Furthermore, the electrostatic potential maps of CuPc-DFP-nOH-Cu ($n = 0, 2$, and 4) reveal distinct partial negative charges localized on the Cu-salphen unit, while partial positive charges accumulate around the hydroxyl groups (Figures S28–S30, Supporting Information), suggesting the potential for CO₂ migration subsequent to its initial adsorption on the hydroxyl groups toward the Cu-salphen unit possessing more negative charges.^[46] The interaction with CO₂ is further corroborated by the differential charge density for CO₂-adsorbed CuPc-DFP-4OH-Cu (Figure S31, Supporting Information).^[47]

Furthermore, density functional theory (DFT) calculations were conducted to study the underlying mechanism. As mentioned above, the main electrocatalytic CO₂RR products of CuPc-DFP-nOH-Cu ($n = 0, 2$, and 4) are CH₄ and C₂H₄, and the FE_{CH₄} decreases along with the enhanced FE_{C₂H₄} from CuPc-DFP-Cu to CuPc-DFP-4OH-Cu. Thus, the intermediate models for the formation of CH₄ and C₂H₄ are presented in Figures S32–S37 (Supporting Information). Based on above in situ tests, it could be deduced that the *CO pathways for CH₄ are occurred on CuPc-DFP-nOH-Cu ($n = 0, 2$, and 4), including the generation of intermediates, such as *CO₂, *COOH, *CO, *CHO, *CHOH, *CH₂OH, *CH₃OH, *CH₃ and *CH₄, during the multi-step proton-electron transfer processes (Figure 6d and Figures S32–S34, Supporting Information).^[48] As for the

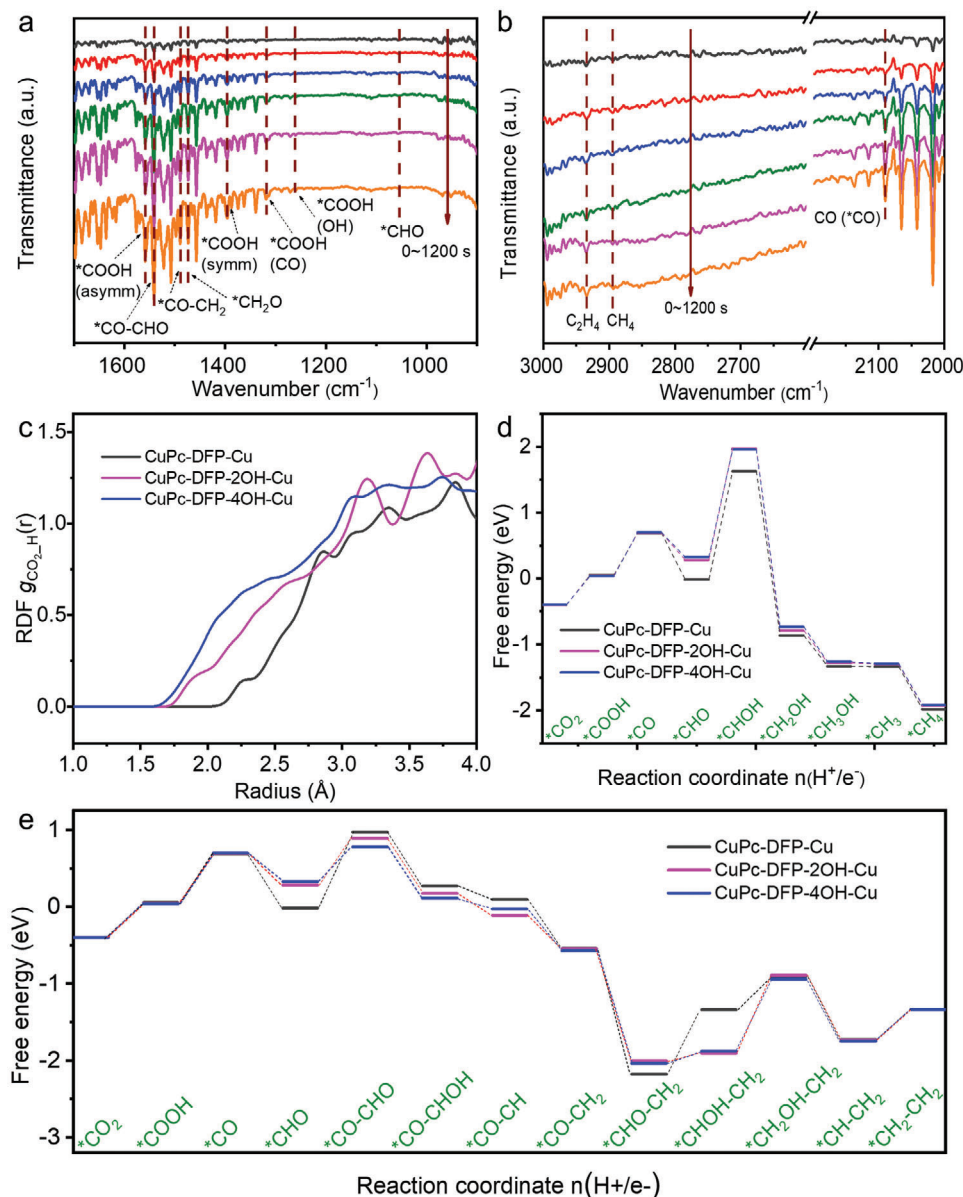


Figure 6. In situ ATR-FTIR spectra and DFT calculations of electrocatalytic CO₂RR. (a) In situ ATR-FTIR spectra of CuPc-DFP-4OH-Cu during the electrocatalytic CO₂RR (range, 1700–900 cm⁻¹). (b) In situ ATR-FTIR spectra of CuPc-DFP-4OH-Cu during the electrocatalytic CO₂RR (range, 3000–2000 cm⁻¹). (c) Radial distribution function of CO₂ on CuPc-DFP-nOH-Cu ($n = 0, 2$, and 4). (d) Free energy profiles of CO₂-to-CH₄ reaction pathway on CuPc-DFP-nOH-Cu ($n = 0, 2$, and 4). (e) Free energy profiles of CO₂-to-C₂H₄ reaction pathway on CuPc-DFP-nOH-Cu ($n = 0, 2$, and 4).

formation mechanism of C₂H₄, we propose a possible electrochemical pathway based on reported references (Figures S35–S37, Supporting Information).^[44,48] Initially, CO₂ is adsorbed and enriched with the assistance of hydroxyl-induced catalytic well, and then is activated on the Cu center of Cu salphen units, which are quickly transformed into *COOH. After that, the *COOH → *CO → *CHO → *CO-CHO → *CO-CHOH → *CO-CH → *CO-CH₂ → *CHO-CH₂ → *CHOH-CH₂ → *CH₂OH-CH₂ → *CH-CH₂ → *CH₂-CH₂ (*represents the catalytic site) occur, involving multi-step proton-electron transfer processes (Figure 6e). Finally, the produced C₂H₄ is desorbed to finish the electrocatalysis process (Figure 6e).

For the generation of both CH₄ and C₂H₄, the generated *CO during the multi-step proton-electron transfer processes is a similar and important intermediate (Figure 6d,e). After that, two possible competitive mechanisms are presented. For the CH₄ production, *CO is hydrogenated to generate *CHO and further *CHOH, which lead to CH₄ pathway.^[41,48] The rate-determining steps (RDS) of this pathway is hydrogenation of *CHO to form *CHOH based on the calculation results. For the C₂H₄ production, the coupling reaction between *CO and subsequently generate *CHO happens, and *CO-CHO as the vital intermediate can be further transformed into C₂H₄.^[44,48] During this process, the RDS is coupling of *CO with *CHO for the

formation of $^*CO-CHO$. For CuPc-DFP-Cu ($\Delta G = 0.59$ eV), it displays the lowest energy barrier for the formation of *CHOH when compared with CuPc-DFP-4OH-Cu and CuPc-DFP-2OH-Cu, suggesting the generation of CH_4 is easier on CuPc-DFP-Cu (Figure 6d). For CuPc-DFP-4OH-Cu ($\Delta G = 0.64$ eV), it displays the lowest energy barrier for the RDS of $^*CO-CHO$ formation in C_2H_4 when compared with CuPc-DFP-2OH-Cu and CuPc-DFP-Cu (Figure 6e). These results comply with the above-mentioned experimental results and reveal that the vital roles of hydroxyl-induced catalytic well in facilitating the electrocatalytic CO_2RR into C_2H_4 .

3. Conclusion

In summary, we have successfully designed a series of Cu-salphen based COFs (CuPc-DFP-nOH-Cu, $n = 0, 2$, and 4) featuring varying levels of hydroxyl-induced catalytic well for selective electrocatalytic CO_2RR . The well-designed catalytic well, achieved by multi-hydroxyl groups, presents strong confinement effects that enable selective adsorption/enrichment/activation of CO_2 , intermediate stabilization, and reduction of energy barriers for electrocatalytic CO_2RR . Notably, the products can be well tuned from CH_4 to C_2H_4 by introducing different levels of catalytic well, in which CuPc-DFP-4OH-Cu with the strongest catalytic well effect exhibits a high 56.86% $FE_{C_2H_4}$ at -0.7 V, meanwhile CuPc-DFP-Cu with the weakest catalytic well effect presents a 75.24% FE_{CH_4} at -1.0 V. Moreover, the pivotal roles of hydroxyl-induced catalytic well with confinement effects have been comprehensively investigated in conjunction with theoretical calculations. This study holds promise for offering novel insights into the development of porous crystalline electrocatalysts for electrocatalytic CO_2RR into C_{2+} products.

4. Experimental Section

Syntheses of CuPc-DFP-nOH ($n = 0, 2$, and 4): For the preparation of CuPc-DFP-4OH, CuPc-8NH₂ (35 mg, 0.05 mmol) and 2, 4-dimethoxyphenylporphyrin (DPP-2OH) (23.7 mg, 0.13 mmol) was added to a Pyrex tube (o.d. \times length, 19 \times 65 mm), then mesitylene (1.5 mL) and 1,4-dioxane (0.5 mL) were added, after sonicating for 15 min, triethylamine (0.25 mL) was added and mixed. After that, the tube was flash frozen by liquid N₂ and degassed by three freeze-pump-thaw cycles and achieved an internal pressure of ≈ 100 mTorr. After that, the mixture was heated at 80 °C for 72 h. A dark green precipitate was obtained and washed with tetrahydrofuran (THF). The obtained sample was washed with THF in a Soxhlet extractor for 48 h. Finally, the product was activated by evacuating under a dynamic vacuum overnight at 80 °C (40.5 mg). The synthesis of CuPc-DFP-nOH ($n = 0$ and 2) was carried out following the same protocol as that of CuPc-DFP-4OH except that the 2-Hydroxy-1,3-benzenedicarboxaldehyde (DPP-2OH) was replaced with 2,6-diformylphenol (DPP) (17.94 mg, 0.13 mmol), 2,4-dihydroxyresorcinolaldehyde (DPP-OH) (20 mg, 0.13 mmol).

Syntheses of CuPc-DFP-nOH-Cu ($n = 0, 2$, and 4): CuPc-DFP-4OH-Cu was synthesized based on reported literatures^[53,54] with modified procedures. CuPc-DFP-4OH (50.0 mg) and Cu(OAc)₂·H₂O (25.0 mg) were first added in a 50 mL three-neck flask, then 20 mL MeOH was added. After stirring for 24 h, the suspension was filtrated and washed with methanol (60 mL) and water (60 mL). Finally, the product was evacuated at 80 °C overnight to obtain dark green solid. The syntheses of CuPc-DFP-nOH-Cu ($n = 0$ and 2) was carried out following the same protocol as that of CuPc-DFP-4OH-Cu.

The Preparation of Working Electrode: Five milligrams of sample was dispersed in a mixed solution of water (200 μ L), 50 μ L Nafion solution (5 wt%), and ethanol (250 μ L). Then it was sonicated for 30 min to obtain a uniform suspension liquid. After that, the 50 μ L catalyst ink was spray-coated on a hydrophobic carbon paper (1 cm \times 2 cm; coatings area, 0.5 \times 1 cm²; loading, ≈ 1 mg cm⁻²), then it was dried at room temperature.

Supporting Information

Supporting Information is available from the Wiley Online Library or from the author.

Acknowledgements

This work was financially supported by the National Key R&D Program of China (2023YFA1507204), National Natural Science Foundation of China (Grants 22475074, 22171139, 22225109, 22309054, 22071109, 22371080, 22301139), Natural Science Foundation of Guangdong Province (No. 2023B1515020076), China Postdoctoral Science Foundation (No. 2023M731154), China National Postdoctoral Program for Innovative Talents (BX20220116), Natural Science Foundation of Jiangsu Province (Grant No. BK 20230375). This work was also supported by the Scientific Research Innovation Project of the Graduate School of South China Normal University.

Conflict of Interest

The authors declare no conflict of interest.

Author Contributions

Y.-L.Y., Q.L., and P.L. contributed equally to this work. Y.-Q.L., Y.C., Y.-R.W., F.Y., and Y.-L.Y. conceived and designed the idea. Y.-L.Y., Q.L., and P.L. designed the experiments, Y.-L.Y. collected and analyzed the data. Q.X., Q.-Y.Z., Y.-X.C., Y.-Q.Y., and H.-T.Y. assisted with the experiments and characterizations. Y.-L.Y. wrote the manuscript. Y.-L.Y., Y.C., Y.-R.W., F.Y., and Y.-Q.L. discussed the results and prepared the manuscript. All the authors reviewed and contributed to this paper.

Data Availability Statement

The data that support the findings of this study are available in the supplementary material of this article.

Keywords

catalytic well, covalent-organic-framework, electrocatalytic CO_2 reduction, ethylene

Received: October 16, 2024
Revised: November 12, 2024
Published online:

- [1] J.-D. Yi, R. Xie, Z.-L. Xie, G.-L. Chai, T.-F. Liu, R.-P. Chen, Y.-B. Huang, R. Cao, *Angew. Chem., Int. Ed.* **2020**, *59*, 23641.
- [2] D. D. Zhu, J. L. Liu, S. Z. Qiao, *Adv. Mater.* **2016**, *28*, 3423.
- [3] D. Yang, J. Wang, Q. Wang, Z. Yuan, Y. Dai, C. Zhou, X. Wan, Q. Zhang, Y. Yang, *ACS Nano* **2022**, *16*, 15681.

- [4] P.-P. Yang, M.-R. Gao, *Chem. Soc. Rev.* **2023**, 52, 4343.
- [5] J. Liu, F. You, B. He, Y. Wu, D. Wang, W. Zhou, C. Qian, G. Yang, G. Liu, H. Wang, Y. Guo, L. Gu, L. Feng, S. Li, Y. Zhao, *J. Am. Chem. Soc.* **2022**, 144, 12410.
- [6] F. S. Roberts, K. P. Kuhl, A. Nilsson, *Angew. Chem., Int. Ed.* **2015**, 54, 5179.
- [7] Y. Gu, J. Li, L. Wang, M. Xie, X. Wu, F. Xie, M. P. Ryan, *Chem. Select* **2019**, 4, 10995.
- [8] H. Mistry, A. S. Varela, C. S. Bonifacio, I. Zegkinoglou, I. Sinev, Y.-W. Choi, K. Kisslinger, E. A. Stach, J. C. Yang, P. Strasser, B. R. Cuenya, *Nat. Commun.* **2016**, 7, 12123.
- [9] T. T. H. Hoang, S. Verma, S. Ma, T. T. Fister, J. Timoshenko, A. I. Frenkel, P. J. A. Kenis, A. A. Gewirth, *J. Am. Chem. Soc.* **2018**, 140, 5791.
- [10] J. Jiao, R. Lin, S. Liu, W.-C. Cheong, C. Zhang, Z. Chen, Y. Pan, J. Tang, K. Wu, S.-F. Hung, H. M. Chen, L. Zheng, Q. Lu, X. Yang, B. Xu, H. Xiao, J. Li, D. Wang, Q. Peng, C. Chen, Y. Li, *Nat. Chem.* **2019**, 11, 222.
- [11] C. Xiao, J. Zhang, *ACS Nano* **2021**, 15, 7975.
- [12] K. Seob Song, P. W. Fritz, D. F. Abbott, L. Nga Poon, C. M. Caridade, F. Gándara, V. Mougél, A. Coskun, *Angew. Chem., Int. Ed.* **2023**, 62, 202309775.
- [13] X. Zhang, X. Yan, P. Chen, P. Zhang, X. Kang, J. Ma, C. Chen, B. Han, *Angew. Chem., Int. Ed.* **2023**, 63, 202315822.
- [14] J. Li, Z. Zhang, W. Hu, *Energy Environ. Mater.* **2022**, 5, 1008.
- [15] J.-M. Seo, H.-J. Noh, J.-P. Jeon, H. Kim, G.-F. Han, S. K. Kwak, H. Y. Jeong, L. Wang, F. Li, J.-B. Baek, *J. Am. Chem. Soc.* **2022**, 144, 19973.
- [16] C. Li, Z. Guo, Z. Liu, T. Zhang, H. Shi, J. Cui, M. Zhu, L. Zhang, H. Li, H. Li, C. Li, *ACS Catal.* **2023**, 13, 16114.
- [17] J.-J. Lv, R. Yin, L. Zhou, J. Li, R. Kikas, T. Xu, Z.-J. Wang, H. Jin, X. Wang, S. Wang, *Angew. Chem., Int. Ed.* **2022**, 61, 202207252.
- [18] S. Overa, B. H. Ko, Y. Zhao, F. Jiao, *Acc. Chem. Res.* **2022**, 55, 638.
- [19] D. Wakerley, S. Lamaison, J. Wicks, A. Clemens, J. Feaster, D. Corral, S. A. Jaffer, A. Sarkar, M. Fontecave, E. B. Duoss, S. Baker, E. H. Sargent, T. F. Jaramillo, C. Hahn, *Nat. Energy* **2022**, 7, 130.
- [20] Y. Wang, J. Liu, G. Zheng, *Adv. Mater.* **2021**, 33, 2005798.
- [21] M. Jun, J. Kundu, D. H. Kim, M. Kim, D. Kim, K. Lee, S.-I. Choi, *Adv. Mater.* **2024**, 36, 2313028.
- [22] B. Chang, H. Pang, F. Raziq, S. Wang, K.-W. Huang, J. Ye, H. Zhang, *Energ. Environ. Sci.* **2023**, 16, 4714.
- [23] W. Lai, Y. Qiao, Y. Wang, H. Huang, *Adv. Mater.* **2023**, 35, 2306288.
- [24] F. Kang, X. Wang, C. Chen, C.-S. Lee, Y. Han, Q. Zhang, *J. Am. Chem. Soc.* **2023**, 145, 15465.
- [25] S. Kandambeth, D. B. Shinde, M. K. Panda, B. Lukose, T. Heine, R. Banerjee, *Angew. Chem., Int. Ed.* **2013**, 52, 13052.
- [26] Q. Gu, J. Zha, C. Chen, X. Wang, W. Yao, J. Liu, F. Kang, J. Yang, Y. Y. Li, D. Lei, Z. Tang, Y. Han, C. Tan, Q. Zhang, *Adv. Mater.* **2024**, 36, 2306414.
- [27] R. Zhao, T. Wang, J. Li, Y. Shi, M. Hou, Y. Yang, Z. Zhang, S. Lei, *Nano Res.* **2023**, 16, 8570.
- [28] H. Guo, D.-H. Si, H.-J. Zhu, Z.-A. Chen, R. Cao, Y.-B. Huang, *Angew. Chem., Int. Ed.* **2024**, 63, 202319472.
- [29] Y. Zhang, X. Zhang, L. Jiao, Z. Meng, H.-L. Jiang, *J. Am. Chem. Soc.* **2023**, 145, 24230.
- [30] X.-F. Qiu, J.-R. Huang, C. Yu, Z.-H. Zhao, H.-L. Zhu, Z. Ke, P.-Q. Liao, X.-M. Chen, *Angew. Chem., Int. Ed.* **2022**, 61, 202206470.
- [31] Z. Zhou, L. Zhang, Y. Yang, I. J. Vitorica-Yrezabal, H. Wang, F. Tan, L. Gong, Y. Li, P. Chen, X. Dong, Z. Liang, J. Yang, C. Wang, Y. Hong, Y. Qiu, A. Götzhäuser, X. Chen, H. Qi, S. Yang, W. Liu, J. Sun, Z. Zheng, *Nat. Chem.* **2023**, 15, 841.
- [32] M. Liu, S. Yang, X. Yang, C.-X. Cui, G. Liu, X. Li, J. He, G. Z. Chen, Q. Xu, G. Zeng, *Nat. Commun.* **2023**, 14, 3800.
- [33] Q.-J. Wu, J. Liang, Y.-B. Huang, R. Cao, *Acc. Chem. Res.* **2022**, 55, 2978.
- [34] X. Zhao, P. Pachfule, A. Thomas, *Chem. Soc. Rev.* **2021**, 50, 6871.
- [35] C. Wang, Z. Lv, W. Yang, X. Feng, B. Wang, *Chem. Soc. Rev.* **2023**, 52, 1382.
- [36] Z. Chen, N. Li, Q. Zhang, *Small Struct.* **2024**, n/a, 2300495.
- [37] F. Meng, S. Bi, Z. Sun, D. Wu, F. Zhang, *Angew. Chem., Int. Ed.* **2022**, 61, 202210447.
- [38] B. Hou, S. Yang, K. Yang, X. Han, X. Tang, Y. Liu, J. Jiang, Y. Cui, *Angew. Chem., Int. Ed.* **2021**, 60, 6086.
- [39] X.-Y. Dong, Y.-N. Si, Q.-Y. Wang, S. Wang, S.-Q. Zang, *Adv. Mater.* **2021**, 33, 2101568.
- [40] H. Wang, X. Bi, Y. Yan, Y. Zhao, Z. Yang, H. Ning, M. Wu, *Adv. Funct. Mater.* **2023**, 33, 2214946.
- [41] Y.-R. Wang, H.-M. Ding, X.-Y. Ma, M. Liu, Y.-L. Yang, Y. Chen, S.-L. Li, Y.-Q. Lan, *Angew. Chem., Int. Ed.* **2022**, 61, 202114648.
- [42] W.-F. Xiong, D.-H. Si, H.-F. Li, X. Song, T. Wang, Y.-B. Huang, T.-F. Liu, T. Zhang, R. Cao, *J. Am. Chem. Soc.* **2024**, 146, 289.
- [43] L. Huang, Z. Liu, G. Gao, C. Chen, Y. Xue, J. Zhao, Q. Lei, M. Jin, C. Zhu, Y. Han, J. S. Francisco, X. Lu, *J. Am. Chem. Soc.* **2023**, 145, 26444.
- [44] R. Xu, D.-H. Si, S.-S. Zhao, Q.-J. Wu, X.-S. Wang, T.-F. Liu, H. Zhao, R. Cao, Y.-B. Huang, *J. Am. Chem. Soc.* **2023**, 145, 8261.
- [45] S. Geng, X. Zhao, Q. Xu, B. Yuan, Y. Wang, M. Liao, L. Ye, S. Wang, Z. Ouyang, L. Wu, Y. Wang, C. Ma, X. Zhao, H. Sun, *Nat. Commun.* **2024**, 15, 944.
- [46] Y. Wu, Q. Hu, H. Liang, A. Wang, H. Xu, L. Wang, X. He, *Adv. Energy Mater.* **2023**, 13, 2300259.
- [47] Y. Chai, Y. Kong, M. Lin, W. Lin, J. Shen, J. Long, R. Yuan, W. Dai, X. Wang, Z. Zhang, *Nat. Commun.* **2023**, 14, 6168.
- [48] S. Osella, W. A. Goddard Iii, *J. Am. Chem. Soc.* **2023**, 145, 21319.
- [49] M. Liu, Y.-R. Wang, H.-M. Ding, M. Lu, G.-K. Gao, L.-Z. Dong, Q. Li, Y. Chen, S.-L. Li, Y.-Q. Lan, *Sci. Bull.* **2021**, 66, 1659.
- [50] Y.-L. Yang, Y.-R. Wang, G.-K. Gao, M. Liu, C. Miao, L.-Y. Li, W. Cheng, Z.-Y. Zhao, Y. Chen, Z. Xin, S.-L. Li, D.-S. Li, Y.-Q. Lan, *Chin. Chem. Lett.* **2022**, 33, 1439.
- [51] H. Dong, M. Lu, Y. Wang, H.-L. Tang, D. Wu, X. Sun, F.-M. Zhang, *Appl. Catal. B Environ.* **2022**, 303, 120897.
- [52] L. Ma, W. Hu, B. Mei, H. Liu, B. Yuan, J. Zang, T. Chen, L. Zou, Z. Zou, B. Yang, Y. Yu, J. Ma, Z. Jiang, K. Wen, H. Yang, *ACS Catal.* **2020**, 10, 4534.
- [53] L. Yuan, L. Zhang, X.-X. Li, J. Liu, J.-J. Liu, L.-Z. Dong, D.-S. Li, S.-L. Li, Y.-Q. Lan, *Chinese Chem. Lett.* **2023**, 34, 107146.
- [54] X. Tian, X. Huang, J.-W. Shi, J. Zhou, C. Guo, R. Wang, Y.-R. Wang, M. Lu, Q. Li, Y. Chen, S.-L. Li, Y.-Q. Lan, *CCS Chem* **2023**, 5, 2557.